

1 **Tropopause Evolution in a Rapidly Intensifying Tropical Cyclone: A Static**  
2 **Stability Budget Analysis in an Idealized, Axisymmetric Framework**

3 Patrick Duran\* and John Molinari

4 *University at Albany, State University of New York, Albany, NY*

5 \**Corresponding author address:* Department of Atmospheric and Environmental Sciences, Univer-  
6 sity at Albany, State University of New York, 1400 Washington Avenue, Albany, NY.

7 E-mail: pduran2008@gmail.com

## ABSTRACT

8 Large changes in tropopause-layer static stability are observed during the  
9 rapid intensification (RI) of an idealized, axisymmetric tropical cyclone (TC).  
10 Over the eye, static stability near the tropopause decreases and the cold-point  
11 tropopause height rises by up to 4 km at the storm center. Outside of the eye,  
12 static stability increases considerably just above the cold-point tropopause,  
13 and the tropopause remains near its initial level.

14 A budget analysis reveals that advection contributes to the static stability  
15 tendencies at all times throughout the upper troposphere and lower strato-  
16 sphere. Within the eye, differential advection plays a particularly impor-  
17 tant role in destabilizing the layer near and above the cold-point tropopause.  
18 Outside of the eye, a radial-vertical circulation develops during RI, with  
19 strong outflow below the tropopause and weak inflow above. Vertical wind  
20 shear above and below the upper-tropospheric outflow maximum induces tur-  
21 bulence, which provides forcing for both destabilization and stabilization  
22 in the tropopause layer. Meanwhile, as organized convection reaches the  
23 tropopause, radiative heating tendencies at the top of the cirrus canopy gen-  
24 erally act to destabilize the upper troposphere and stabilize the lower strato-  
25 sphere. Turbulent mixing and radiative heating combine to play an important  
26 role in the development of the strong stable layer immediately above the cold-  
27 point tropopause during RI. The results suggest that turbulence and radiation,  
28 alongside advection, play fundamental roles in the upper-level static stability  
29 evolution of TCs.

## 30 **1. Introduction**

31 Using a high-resolution dropsonde dataset collected during the Tropical Cyclone Intensity ex-  
32 periment (TCI; Doyle et al. 2017), Duran and Molinari (2018) observed dramatic changes in  
33 tropopause structure during the rapid intensification (RI) of Hurricane Patricia (2015). The goal of  
34 the present paper is to analyze the processes that might have produced the upper-tropospheric and  
35 lower-stratospheric fluctuations observed in Patricia using an idealized axisymmetric simulation.

36 After undergoing a remarkably rapid intensification (RI), Hurricane Patricia (2015) set a new  
37 record as the strongest tropical cyclone (TC) ever observed in the Western Hemisphere (Kimber-  
38 lain et al. 2016; Rogers et al. 2017). TCI dropsonde observations collected during this RI period  
39 revealed dramatic changes in the cold-point tropopause height and upper-level static stability (Du-  
40 ran and Molinari 2018). In particular, when Patricia was at tropical storm intensity shortly before  
41 RI commenced, a strong inversion layer existed just above the cold-point tropopause. During the  
42 first half of the RI period, this inversion layer weakened throughout Patricia’s inner core, with the  
43 weakening most pronounced over the developing eye. By the time the storm reached its maximum  
44 intensity of  $95 \text{ m s}^{-1}$ , the inversion layer over the eye had disappeared almost completely, which  
45 was accompanied by a greater than 1-km increase in the tropopause height. Meanwhile over the  
46 eyewall region, the static stability increased and the tropopause remained near its initial level.

47 Despite the importance of tropopause-layer thermodynamics in theoretical models of hurri-  
48 canes (Emanuel and Rotunno 2011; Emanuel 2012), most observational studies of the upper-  
49 tropospheric structure of TCs are decades old. Recently, however, Komaromi and Doyle (2017)  
50 found that stronger TCs tended to have a higher and warmer tropopause over their inner core than  
51 weaker TCs. Their results are consistent with the evolution observed over the inner core of Hur-

52 ricane Patricia, in which the tropopause height increased and the tropopause temperature warmed  
53 throughout RI (Duran and Molinari 2018).

54 Idealized simulations of a TC analyzed by Ohno and Satoh (2015) suggested that the develop-  
55 ment of an upper-level warm core near the 13-km level acted to decrease the static stability near the  
56 tropopause within the eye (compare their Figs. 9,10). Although the mechanisms that might drive  
57 this static stability evolution have not been examined explicitly, Stern and Zhang (2013) described  
58 the development of the TC warm core using a potential temperature ( $\theta$ ) budget analysis. They  
59 found that radial and vertical advection both played important roles in warm core development  
60 throughout RI, and subgrid-scale diffusion became particularly important during the later stage of  
61 RI.

62 Other processes that can modify the static stability in the upper troposphere of TCs include  
63 radiative heating within and near the top of the cirrus canopy and shear-induced turbulent mixing  
64 near the outflow jet. To our knowledge, the only paper that has examined explicitly the static  
65 stability evolution in a modeled TC is Kepert et al. (2016), but their analysis was limited to the  
66 boundary layer. The analysis herein is based upon that of Stern and Zhang (2013), except using a  
67 static stability budget similar to that of Kepert et al. (2016), with a focus on the upper troposphere  
68 and lower stratosphere.

## 69 **2. Model Setup**

70 The numerical simulations were performed using version 19.4 of Cloud Model 1 (CM1) de-  
71 scribed in Bryan and Rotunno (2009). The equations of motion were integrated on a 3000-km-  
72 wide, 30-km-deep axisymmetric grid with 1-km horizontal and 250-m vertical grid spacing. The  
73 computations were performed on an  $f$ -plane at 15°N latitude, over a sea surface with constant  
74 temperature of 30.5°C, which matches that observed near Hurricane Patricia (2015; Kimberlain

et al. 2016). Horizontal turbulence was parameterized using the Smagorinsky scheme described in Bryan and Rotunno (2009, pg. 1773), with a prescribed mixing length that varied linearly from 100 m at a surface pressure of 1015 hPa to 1000 m at a surface pressure of 900 hPa. Vertical turbulence was parameterized using the formulation of Markowski and Bryan (2016, their Eq. 6), using an asymptotic vertical mixing length of 100 m. A Rayleigh damping layer was applied outside of the 2900-km radius and above the 25-km level to prevent spurious gravity wave reflection at the model boundaries. Microphysical processes were parameterized using the Thompson et al. (2004) scheme and radiative heating tendencies were computed every two minutes using the Rapid Radiative Transfer Model for GCMs (RRTMG) longwave and shortwave schemes (Iacono et al. 2008). The initial temperature and humidity field was horizontally homogeneous and determined by averaging all Climate Forecast System Reanalysis (CFSR) grid points within 100 km of Patricia's center of circulation at 18 UTC 21 October 2015. The vortex described in Rotunno and Emanuel (1987, their Eq. 37) was used to initialize the wind field, setting all parameters equal to the values used therein.

Although hurricanes simulated in an axisymmetric framework tend to be more intense than those observed in nature, the intensity evolution of this simulation matches reasonably well with that observed in Hurricane Patricia. After an initial spin-up period of about 20 hours, the modeled storm (Fig. 1, blue lines) began an RI period that lasted approximately 30 hours. After this RI, the storm continued to intensify more slowly until the maximum 10-m wind speed reached  $89 \text{ m s}^{-1}$  and the sea-level pressure reached its minimum of 846 hPa 81 hours into the simulation. Hurricane Patricia (red stars) exhibited a similar intensity evolution prior to its landfall, with an RI period leading to a maximum 10-m wind speed of  $95 \text{ m s}^{-1}$  and a minimum sea-level pressure of 872 hPa.

### 97 3. Budget Computation

98 The static stability can be expressed as the squared Brunt-Väisälä frequency:

$$N_m^2 = \frac{g}{T} \left( \frac{\partial T}{\partial z} + \Gamma_m \right) \left( 1 + \frac{T}{R_d/R_v + q_s} \frac{\partial q_s}{\partial T} \right) - \frac{g}{1 + q_t} \frac{\partial q_t}{\partial z}, \quad (1)$$

99 where  $g$  is gravitational acceleration,  $T$  is temperature,  $R_d$  and  $R_v$  are the gas constants of dry air  
100 and water vapor, respectively,  $q_s$  is the saturation mixing ratio,  $q_t$  is the total condensate mixing  
101 ratio, and  $\Gamma_m$  is the moist-adiabatic lapse rate:

$$\Gamma_m = g(1 + q_t) \left( \frac{1 + L_v q_s / R_d T}{c_{pm} + L_v \partial q_s / \partial T} \right), \quad (2)$$

102 where  $L_v$  is the latent heat of vaporization and  $c_{pm}$  is the specific heat of moist air at constant  
103 pressure. In the tropopause layer,  $q_s$ ,  $\partial q_s / \partial T$ , and  $\partial q_t / \partial z$  approach zero. In this limiting case,  
104 Eq. 1 reduces to:

$$N^2 = \frac{g}{\theta} \frac{\partial \theta}{\partial z}, \quad (3)$$

105 where  $\theta$  is the potential temperature.

106 To compute  $N^2$ , CM1 uses Eq. 1 in saturated environments and Eq. 3 in sub-saturated envi-  
107 ronments. For simplicity, however, only Eq. 3 will be employed for the budget computations  
108 throughout the entire domain<sup>1</sup>.

109 Taking the time derivative of Eq. 3 yields the static stability tendency:

$$\frac{\partial N^2}{\partial t} = \frac{g}{\theta} \frac{\partial}{\partial z} \frac{\partial \theta}{\partial t} - \frac{g}{\theta^2} \frac{\partial \theta}{\partial z} \frac{\partial \theta}{\partial t}, \quad (4)$$

110 where the potential temperature tendency,  $\partial \theta / \partial t$ , can be written, following Bryan (cited 2018):

$$\frac{\partial \theta}{\partial t} = -u \frac{\partial \theta}{\partial r} - w \frac{\partial \theta}{\partial z} + HTURB + VTURB + MP + RAD + DISS \quad (5)$$

111 Each term on the right-hand side of Eq. 5 represents a  $\theta$  budget variable, each of which is output  
112 directly by the model every minute.

---

<sup>1</sup>The validity of this approximation will be substantiated later in this section.

113 The first term on the right-hand side of Eq. 4 is larger than the second term throughout most of  
 114 the tropopause layer (not shown). Consequently, the contribution of each of the terms in Eq. 5 to  
 115 the  $N^2$  tendency can be interpreted in light of a vertical gradient of each term.

116 Taking the vertical gradient of the first two terms on the right-hand side of Eq. 5 yields the time  
 117 tendency of the vertical  $\theta$  gradient due to horizontal and vertical advection<sup>2</sup>:

$$\left( \frac{\partial}{\partial t} \frac{\partial \theta}{\partial z} \right)_{adv} = -u \frac{\partial}{\partial r} \frac{\partial \theta}{\partial z} - w \frac{\partial}{\partial z} \frac{\partial \theta}{\partial z} - \frac{\partial u}{\partial z} \frac{\partial \theta}{\partial r} - \frac{\partial w}{\partial z} \frac{\partial \theta}{\partial z}. \quad (6)$$

118 The first two terms on the right-hand side of Eq. 6 represent advection of static stability by the  
 119 radial and vertical wind, respectively. These terms act to rearrange the static stability field, but  
 120 cannot strengthen or weaken static stability maxima or minima. The third and fourth terms on  
 121 the right-hand side of Eq. 6 represent, respectively, the tilting of isentropes in the presence of  
 122 vertical wind shear, and the stretching or squashing of isentropes by vertical gradients of vertical  
 123 velocity. Since these terms involve velocity gradients, they can act to strengthen or weaken static  
 124 stability maxima or minima through differential advection. Unless otherwise stated, any reference  
 125 to "advection" in this paper indicates the sum of all of the terms in Eq. 6.

126 Returning to Eq. 5, HTURB and VTURB are the  $\theta$  tendencies from the horizontal and vertical  
 127 turbulence parameterizations, MP is the tendency from the microphysics scheme, RAD is the  
 128 tendency from the radiation scheme, and DISS is the tendency due to turbulent dissipation. This  
 129 equation neglects Rayleigh damping, since the entire analysis domain lies outside of the regions  
 130 where damping is applied. Each term in Eq. 5 is substituted for  $\partial \theta / \partial t$  in Eq. 4, yielding the  
 131 contribution of each budget term to the static stability tendency. These terms are summed, yielding  
 132 an instantaneous "budget change" in  $N^2$  every minute. The budget changes are then averaged over

---

<sup>2</sup>These terms include the tendencies due to implicit diffusion in the fifth-order finite differencing scheme, which are separated from the advection terms in the CM1 budget output

133 24-hour periods and compared to the total model change in  $N^2$  over that same time period, i.e.:

$$\Delta N_{budget}^2 = \frac{1}{\delta t} \sum_{t=t_0}^{t_0+\delta t} \left. \frac{\partial N^2}{\partial t} \right|_t \quad (7)$$

$$\Delta N_{model}^2 = N_{t_0+\delta t}^2 - N_{t_0}^2 \quad (8)$$

$$Residual = \Delta N_{model}^2 - \Delta N_{budget}^2 \quad (9)$$

136 where  $t_0$  is an initial time and  $\delta t$  is 24 hours.

137 Eqs. 7-9 are plotted for three consecutive 24-hour periods in Fig. 2. For this and all subsequent  
 138 radial-vertical cross sections, a 1-2-1 smoother is applied once in the radial direction to eliminate  
 139  $2\Delta r$  noise that appears in some of the raw model output and calculated fields. The left column  
 140 of Fig. 2 depicts the model changes computed using Eq. 8, together with Eq. 1 in saturated envi-  
 141 ronments and Eq. 3 in subsaturated environments. The center column depicts the budget changes  
 142 computed using Eq. 7 together with Eq. 3 throughout the entire domain. Thus, the left column  
 143 includes the effect of moisture in the  $N^2$  computations, whereas the center column neglects mois-  
 144 ture. The right column depicts the residuals, computed using Eq. 9 (i.e. the left column minus  
 145 the center column.) In every 24-hour period, the budget changes are nearly identical to the model  
 146 changes, which is reflected in the near-zero residuals in the right column. This indicates that the  
 147 budget accurately represents the model variability, which implies that the neglect of moisture in  
 148 the budget computation introduces negligible error within the analysis domain<sup>3</sup>.

149 In the tropopause layer, some of the budget terms are small enough to be ignored. To determine  
 150 which of the budget terms are most important, a time series of the contribution of each of the  
 151 budget terms in Eq. 5 to the tropopause-layer static stability tendency is plotted in Fig. 3. For this  
 152 figure, each of the budget terms is computed using the method described in Section 3, except with

---

<sup>3</sup>This is not the case in the lower- and mid-troposphere, where the residual actually exceeds the budget tendencies in many places, likely due to the neglect of moisture; thus we limit this analysis to the upper troposphere and lower stratosphere.



153 1-hour averaging intervals instead of 24-hour intervals. The absolute values of these tendencies  
154 are then averaged over the radius-height domain of the plots shown in Fig. 2 and plotted as a time  
155 series<sup>4</sup>. Advection (Fig. 3, red line) plays an important role in the mean tropopause-layer static  
156 stability tendency at all times, and vertical turbulence (Fig. 3, blue line) and radiation (Fig. 3, dark  
157 green line) also contribute significantly. The remaining three processes - horizontal turbulence,  
158 microphysics, and dissipative heating - are negligible everywhere outside of the eyewall, and do  
159 not play important roles in the mesoscale tropopause variability.

160 The preceding analysis indicates that, at all times, three budget terms dominate the tropopause-  
161 layer static stability tendency: advection, vertical turbulence, and radiation. Variations in the  
162 magnitude and spatial structure of these terms drive the static stability changes depicted in Fig. 2;  
163 subsequent sections will focus on these variations and what causes them.

## 164 4. Results

### 165 *a. Static stability evolution*

166 The average  $N^2$  over the first day of the simulation (Fig. 4a) indicates the presence of a weak  
167  $N^2$  maximum just above the cold-point tropopause. Over the subsequent 24 hours, during the  
168 RI period, the  $N^2$  within and above this layer decreased within the 25-km radius (Fig. 4b). This  
169 decreasing  $N^2$  corresponded to an increase in the tropopause height within the developing eye,  
170 maximized at the storm center. Outside of the eye, meanwhile, the tropopause height decreased  
171 over the eyewall region (25-60-km radius) and increased only slightly outside of the 60-km ra-  
172 dius. In this outer region, the  $N^2$  maximum just above the tropopause strengthened during RI.

---

<sup>4</sup>It will be seen in subsequent figures that each of the terms contributes both positively and negatively to the  $N^2$  tendency within the analysis domain. Thus, taking an average over the domain tends to wash out the positive and negative contributions. To circumvent this problem, the absolute value of each of the terms is averaged.

173 These trends continued as the storm's intensity leveled off in the 48-72-hour period (Fig. 4c). The  
174 tropopause height increased to nearly 21 km at the storm center and sloped sharply downward to  
175 16.3 km on the inner edge of the eyewall, near the 30 km radius. Static stability outside of the eye,  
176 meanwhile, continued to increase just above the cold-point tropopause. This  $N^2$  evolution closely  
177 follows that observed in Hurricane Patricia (2015; Duran and Molinari 2018, see their Fig. 4). The  
178 mechanisms that led to these  $N^2$  changes will be investigated in the subsequent sections.

## 179 *b. Static stability budget analysis*

### 180 *(i) 0-24 hours*

181 The initial spin-up period was characterized by a steady increase of the maximum wind speed  
182 from 11 m s<sup>-1</sup> to 22 m s<sup>-1</sup> (Fig. 1a, blue line), an intensification rate that closely matched that of  
183 TC Patricia (Fig. 1a, red stars). The weakening of the lower-stratospheric  $N^2$  maximum during  
184 this period is reflected in the total  $N^2$  budget change over this time (Fig. 5a). The layer just above  
185 the cold-point tropopause was characterized by decreasing  $N^2$  (purple shading), maximizing at the  
186 storm center. At and immediately below the tropopause, meanwhile, saw increasing  $N^2$  during this  
187 time period. Although these tendencies extended out to the 200-km radius, they were particularly  
188 pronounced at innermost radii. A comparison of the contributions of advection (Fig. 5b), vertical  
189 turbulence (Fig. 5c), and radiation (Fig. 5d) reveals that advection was the primary driver of the  
190  $N^2$  tendency during this period, acting to stabilize near and just below the tropopause and destabi-  
191 lize above. Although vertical turbulence acted in opposition to advection (i.e. it acted to stabilize  
192 regions that advection acted to destabilize), the magnitude of the advective tendencies was larger,  
193 particularly at the innermost radii. The sum of advection and vertical turbulence (Fig. 5e) almost  
194 exactly replicated the static stability tendencies above the tropopause. Radiative tendencies, mean-  
195 while, (Fig. 5d) acted to destabilize the layer below about 16 km and stabilize the layer between

16 and 17 km. The sum of advection, vertical turbulence, and radiation (Fig. 5f) reproduced the total change in  $N^2$  almost exactly.

(ii) 24-48 hours

During the RI period, the maximum wind speed increased from  $22 \text{ m s}^{-1}$  to  $80 \text{ m s}^{-1}$ . Over this time,  $N^2$  within the eye generally decreased above 16 km and increased below (Fig. 6a), with the destabilization above 16 km maximizing near the level of the mean cold-point tropopause. These tendencies at the innermost radii were driven almost entirely by advection (Fig. 6b). Vertical turbulence (Fig. 6c) and radiation (Fig. 6d) contributed negligibly to the static stability tendencies in this region.

Outside of the eye, the  $N^2$  evolution exhibited alternating layers of positive and negative tendencies. Near and above 18 km existed an upward-sloping region of decreasing  $N^2$  that extended out to the 180-km radius. In this region, neither vertical turbulence nor radiation exhibited negative  $N^2$  tendencies; advection was the only forcing for this destabilization. Immediately below this layer, just above the cold-point tropopause, was a region of increasing  $N^2$  that sloped upward from 17 km near the 30-km radius to just below 18 km outside of the 100-km radius. Advection and vertical turbulence both contributed to this positive  $N^2$  tendency, with advection playing an important role below about 17.5 km and and turbulence playing an important role above. The sum of advection and turbulence (Fig. 6e) reveals two discontinuous regions of increasing  $N^2$  in the 17-18-km layer rather than one contiguous region. The addition of radiation to these two terms, however, (Fig. 6f) provides the link between these two regions, indicating that radiation also plays a role in strengthening the stable layer just above the tropopause. In the 16-17-km layer, just below the cold-point tropopause, a horizontally-extensive layer of destabilization also was forced by a combination of advection, vertical turbulence, and radiation. The sum of advection and vertical turbulence ac-

counts for only a portion of the decreasing  $N^2$  in this layer, and actually indicates forcing for stabilization near the 50-km radius and outside of the 130-km radius. Radiative tendencies overcome this forcing for stabilization in both of these regions to produce the radially-extensive region of destabilization observed just below the tropopause.

The sum of advection, vertical turbulence, and radiation (Fig. 6f) once again closely follows the observed  $N^2$  variability, except in the eyewall region, where the neglect of latent heating and horizontal turbulence introduces some differences.

### (iii) 48-72 hours

After the storm's maximum wind speed leveled off near  $80 \text{ m s}^{-1}$ , the magnitude of the static stability tendencies within the eye decreased to near zero (Fig. 7a).

Outside of the eye, however,  $N^2$  continued to decrease in the layer immediately surrounding the tropopause. The sum of advection and vertical turbulence (Fig. 7e) indicates that the increase of  $N^2$  observed in the 17-18-km layer and inside of the 80-km radius cannot be attributed to these processes, since the sum of these two terms provided forcing for destabilization. Instead, radiation (Fig. 7d) provided the forcing for stabilization in this region. Outside of the 80-km radius, both advection (Fig. 7b) and vertical turbulence (Fig. 7c) provided forcing for stabilization near and just above the 18-km level. The sum of the two terms (Fig. 7e) indicates increasing  $N^2$  near the 18-km level everywhere outside of the 80-km radius, but this stabilization is slightly weaker in the 90-120-km radial band than the observed value. The addition of radiation (Fig. 7f) provided the extra forcing for stabilization required to account for the observed increase in  $N^2$ . Outside of the 120-km radius, the region of radiative forcing for stabilization sloped downward, and the increase in  $N^2$  observed near 18 km can be explained entirely by a combination of advection and vertical turbulence. The layer of decreasing  $N^2$  observed near the tropopause was forced primarily

242 by vertical turbulence and radiation. Within most of this region, advection provided strong forcing  
243 for stabilization, but this forcing was outweighed by the negative  $N^2$  tendencies induced by a  
244 combination of vertical turbulence and radiation.

## 245 5. Discussion

### 246 *a. The role of advection*

247 Advection played an important role in the tropopause-layer  $N^2$  evolution at all stages of intensifi-  
248 cation, but for brevity, this section will focus only on the RI (24-48-hour) period. To investigate the  
249 advective processes more closely, the individual contributions of horizontal and vertical advection  
250 during the RI period are shown in Fig. 8, along with the corresponding time-mean radial and verti-  
251 cal velocities and  $\theta$ . The  $N^2$  tendencies due to the two advective components (Fig. 8a,b) exhibited  
252 strong cancellation, consistent with flow that was nearly isentropic. There existed, however, a  
253 large region near the tropopause in which the total advective tendency was nonzero (Fig. 6b).  
254 These nonzero tendencies were related to the development of the TC's secondary circulation as it  
255 intensified.

256 During the RI period, strong radial and vertical circulations developed near the tropopause  
257 (Fig. 8c,d), which forced high-magnitude  $N^2$  tendencies due to advection (Fig. 8a,b). A layer  
258 of strong outflow formed at and below the tropopause during this period, with the outflow maxi-  
259 mum (dashed cyan line) curving from the 14-km level at the 50-km radius to just below the 16-km  
260 level outside of the 80-km radius (Fig. 8c). Notably, the  $N^2$  tendency due to horizontal advec-  
261 tion (Fig. 8a) tended to switch signs at this line, with stabilization below the outflow maximum  
262 and destabilization above. This is consistent with the outflow layer carrying air with increasingly  
263 large  $\theta$  from the eyewall to large radii as the storm intensified. This increase in  $\theta$  maximized near

the outflow maximum, which acted to decrease  $\partial\theta/\partial z$  above the outflow maximum and increase it below. This mechanism is the same as that discussed in Trier and Sharman (2009), in which vertical wind shear in the outflow layer of a mesoscale convective system acted to modify the upper-tropospheric static stability through differential advection of isentropes.

Meanwhile in the lower stratosphere, a thin layer of  $2\text{--}4\text{ m s}^{-1}$  inflow developed a few hundred meters above the tropopause, similar to that which was observed in Hurricane Patricia (2015; Duran and Molinari 2018) and in previous modeling studies (e.g. Ohno and Satoh 2015; Kieu et al. 2016). Since the isentropes in this layer sloped slightly upward with radius (i.e.  $\partial\theta/\partial r < 0$ ), this inflow acted to import lower  $\theta$  air from outer radii to inner radii. Since the negative  $\theta$  tendencies maximized at the level of maximum inflow, the layer below the inflow maximum destabilized and the layer above stabilized (Fig. 8a).

Curiously, horizontal advection contributed to the  $N^2$  tendency everywhere within the eye, even though the mean radial velocity there was near zero. Close examination of the model output revealed that these tendencies were forced by advective processes associated with inward-propagating waves. Although the radial velocity perturbations induced by these waves averaged out to zero, the advective tendencies forced by the radial velocity perturbations did not. Additionally, when these waves reached  $r=0$ , a dipole of vertical velocity resulted, with ascent above and descent below. For reasons that remain unclear, the regions of ascent were more persistent than the regions of descent, which resulted in the mean ascent observed near  $r=0$  above 17 km in Fig. 8b.

Vertical advection also played an important role in the tropopause-layer static stability evolution. Within the eye, subsidence dominated below 17 km, while mean ascent existed near the storm center above 17 km. Although the magnitude of the subsidence was larger at lower altitudes,  $\partial\theta/\partial z$  was smaller there. Because  $\partial\theta/\partial z$  was smaller, the subsidence at lower levels could not accomplish as much warming as the subsidence at higher levels in the eye, consistent with the

288 results of Stern and Zhang (2013). As a result, vertical advection within the eye acted to stabilize  
289 the layer below 16 km during RI.

290 Outside of the 27-km radius, ascent dominated the troposphere, while a 1.5-km-deep layer of  
291 descent existed immediately above the tropopause. These regions of ascent and descent converged  
292 just above the tropopause; this convergence acted to compact the isentropes in this layer and in-  
293 crease the static stability. Above the lower-stratospheric subsidence maximum, meanwhile, verti-  
294 cal advection acted to decrease  $N^2$ . Below the tropopause, differential vertical advection increased  
295  $N^2$  within the eyewall region and also at larger radii above the vertical velocity maximum at larger  
296 radii. Outside of the eyewall and below the vertical velocity maximum, meanwhile, differential  
297 vertical advection acted to decrease  $N^2$ .

298 Comparing the  $N^2$  tendencies forced by horizontal (Fig. 8a) and vertical (Fig. 8b) advection  
299 to the total advective tendency seen in Fig. 6b reveals that horizontal advective tendencies domi-  
300 nated the troposphere, while vertical advective tendencies dominated the layer near and above the  
301 tropopause. Thus, tilting of isentropes in the vicinity of the upper-tropospheric outflow maximum  
302 appears to be the most important process governing the  $N^2$  tendency in the troposphere, whereas  
303 convergence of vertical velocity appears to be the most important process near the tropopause.

#### 304 *b. The role of radiation*

305 During the initial spin-up period (0-24 hours; Fig. 9a), convection was not deep enough to  
306 deposit large quantities of ice near the tropopause and create a persistent cirrus canopy. Due to the  
307 lack of ice particles, the radiative heating tendencies during this period (Fig. 9b) were relatively  
308 small and confined to the region above a few particularly strong, although transient, convective  
309 towers. During RI (24-48 hours), the eyewall updraft strengthened and a radially-extensive cirrus  
310 canopy developed near the tropopause (Fig. 9c). The enhanced vertical gradient of ice mixing ratio

311 at the top of the cirrus canopy induced strong diurnal-mean radiative cooling near the tropopause  
312 (Fig. 9d). This cooling exceeded  $0.6 \text{ K h}^{-1}$  in some places and sloped downward from the lower  
313 stratosphere into the upper troposphere, following the top of the cirrus canopy. A small radiative  
314 warming maximum also appeared outside of the 140-km radius below this region of cooling. These  
315 results broadly agree with those of Bu et al. (2014; see their Fig. 11a), whose CM1 simulations  
316 produced a  $0.3 \text{ K h}^{-1}$  diurnally-averaged radiative cooling at the top of the cirrus canopy and  
317 radiative warming within the cloud that maximized near the 200-km radius. This broad region  
318 of radiative cooling acted to destabilize the layer below the cooling maximum and stabilize the  
319 layer above, which can be seen in Fig. 6d. The small area of net radiative heating outside of the  
320 140-km radius enhanced the destabilization above 16 km in this region and produced a thin layer  
321 of stabilization in the 15-16-km layer.

322 After the TC's RI period completed (48-72 hours), strong radiative cooling remained near the  
323 tropopause at inner radii (Fig. 9f), sloping downward with the top of the cirrus canopy to below  
324 the tropopause at outer radii. Cooling rates exceeded  $1 \text{ K h}^{-1}$  just above the tropopause between  
325 the 30- and 70-km radii. This value is more than three times the maximum cooling rate of  $0.3 \text{ K h}^{-1}$   
326 observed by Bu et al. (2014), a discrepancy that is a consequence of their larger vertical grid  
327 spacing compared to that used here, along with a contribution from differing radiation schemes. To  
328 compare our results to those of Bu et al. (2014), we ran a simulation identical to that described in  
329 Section 2, except using the NASA-Goddard radiation scheme and 625-m vertical grid spacing, to  
330 match those of Bu et al. (2014). This simulation produced a maximum 24-hour-average radiative  
331 cooling rate of  $0.3 \text{ K h}^{-1}$ , which agrees with that shown in Bu et al. (2014). Another simulation  
332 using 625-m vertical grid spacing and RRTMG radiation produced 24-hour-average cooling rates  
333 of up to  $0.6 \text{ K h}^{-1}$ , which is consistent with the WRF simulations of Bu et al. (2014). This suggests  
334 that vertical grid spacing smaller than 625 m is necessary to resolve properly the radiative cooling



335 at the top of the cirrus canopy, and that the results can be quite sensitive to the radiation scheme  
336 used.

337 Meanwhile below the tropopause, time-mean radiative warming spread from 30- to 160-km  
338 radius within the cirrus canopy. The existence of radiative cooling overlying radiative warming in  
339 this region led to radiatively-forced destabilization at and below the tropopause, as was observed  
340 in Fig. 7d. Beneath the warming layer existed a region of forcing for stabilization, while a much  
341 stronger region of forcing for stabilization existed in the lower stratosphere, above the cooling  
342 maximum.

343 The results herein suggest that radiative heating tendencies played an important role in destabi-  
344 lizing the upper troposphere and stabilizing the lower stratosphere after the cirrus canopy devel-  
345 oped.

### 346 *c. The role of turbulent mixing*

347 Fig. 10 depicts the effect of turbulent mixing on the  $\theta$  profile of an initially stably-stratified  
348 layer. At the initial time in this idealized case,  $\theta$  increases with height at a constant rate (Fig. 10,  
349 left panel). The imposition of turbulence (blue hatching) adjusts the  $\theta$  profile within the mixed  
350 layer toward a constant value equal to the mean value of that layer in the initial state (Fig. 10, right  
351 panel). Just above and just below the mixed layer, however, the  $\theta$  profile remains undisturbed.  
352 Consequently, although turbulent mixing acts to decrease  $\partial\theta/\partial z$  in the layer in which it is occur-  
353 ring, it actually increases  $\partial\theta/\partial z$  just below and just above the layer. These vertical gradients of  
354 turbulent mixing are quite important, particularly on the flanks of the upper-tropospheric outflow  
355 jet.

356 Two distinct maxima of vertical eddy diffusivity developed in the tropopause layer as the storm  
357 intensified (Fig. 11). Comparison of these turbulent regions to the  $N^2$  tendencies in Figs. 6c and

7c reveals that the layers in which vertical eddy diffusivity maximized corresponded to layers of destabilization due to vertical turbulence. Just outside of these layers, however, vertical turbulence acted to increase  $N^2$ . The large vertical gradient of vertical eddy diffusivity near the tropopause played an important role in developing the lower-stratospheric stable layer during RI. This supports the hypothesized role of turbulence in setting the outflow-layer  $\theta$  stratification in Rotunno and Emanuel (1987).

## 6. Conclusions

The simulated  $N^2$  evolution shown herein closely matched that observed during the RI of Hurricane Patricia (2015). Three processes dominated the  $N^2$  variability in the upper troposphere and lower stratosphere: advection, radiation, and vertical turbulence. Radiation and vertical turbulence played particularly important roles in developing the strong  $N^2$  maximum just above the cold-point tropopause during RI.

To put the  $N^2$  variability observed near the tropopause into context, Fig. 12 depicts the model change in  $N^2$  over the RI period from 0 to 21 km altitude, along with the vertical eddy diffusivity and the radiative heating rate. It is clear that the largest changes in  $N^2$  occurred in a relatively shallow layer immediately surrounding the tropopause (Fig. 12a). This shallow layer also contained the largest diurnally-averaged radiative heating tendencies found anywhere in the domain (Fig. 12c). Values of vertical eddy diffusivity larger than any found outside of the boundary layer also resided in the upper troposphere (Fig. 12b). The results herein suggest that this turbulence not only develops as a response to the presence of small static stability and large vertical wind shear, as discussed by Molinari et al. (2014) and Duran and Molinari (2016), but also can actively increase the static stability in highly localized regions just above and below the mixed layers.

380 Since two of the most important processes contributing to the  $N^2$  variability are parameter-  
381 ized, and one (radiation) closely depends on yet another parameterized process (microphysics),  
382 the tropopause-layer  $N^2$  variability could be quite sensitive to the assumptions inherent to the pa-  
383 rameterizations used. A better understanding of the microphysical characteristics of the TC cirrus  
384 canopy, its interaction with radiation, and outflow-layer turbulence is critical to understanding the  
385 tropopause-layer  $N^2$  evolution.

386 In this paper, all of the variables were averaged over a full diurnal cycle to eliminate the effects  
387 of diurnal variability and isolate the overall storm evolution. Diurnal variations in static stability  
388 near the tropopause are potentially of interest with respect to the tropical cyclone diurnal cycle,  
389 and will be the subject of future work.

390 *Acknowledgments.* We are indebted to George Bryan for his continued development and support  
391 of Cloud Model 1. We also thank Jeffrey Kepert, Robert Fovell, and Erika Navarro for helpful  
392 conversations related to this work. This research was supported by NSF Grant #1636799.

## 393 APPENDIX

### 394 Sensitivity experiments

395 The simulations exhibited some sensitivity to the initial thermodynamic profile and the pre-  
396 scribed vertical mixing length. Although the details of the intensification and the tropopause-layer  
397  $N^2$  evolution varied when these quantities were changed, the conclusions of the paper remain  
398 unchanged.

#### 399 *a. Sensitivity to the initial thermodynamic profile*

400 A number of sensitivity experiments were conducted using a variety of initial soundings. Chang-  
401 ing the initial temperature and humidity profiles affected the timing of the onset of organized deep

402 convection and the rapidity of intensification. In all simulations, however, convection eventually  
403 penetrated to the tropopause, at which time vertical turbulence and radiation combined with ad-  
404 vection to adjust the  $N^2$  profile toward that which was observed in the control run. By the end of  
405 the RI period in every simulation, all three processes were actively modifying the  $N^2$  profile near  
406 the tropopause.

407 As an example, 24-hour averages of  $N^2$  are plotted in Fig. A1 for a simulation that was identical  
408 to that used in this paper, except the initial sounding was determined by averaging every CFSR  
409 grid point within 1000 km of TC Patricia's storm center at 18 UTC 21 October 2015 instead of  
410 averaging only within the 100-km radius. Although the lower-stratospheric stable layer developed  
411 more slowly and was weaker than that shown in Fig. 4, the overall evolution was quite similar and  
412 the same budget terms dominated the  $N^2$  evolution.

#### 413 *b. Sensitivity to the vertical mixing length*

414 The rate of turbulent mixing in the Smagorinsky scheme used herein is highly dependent on a  
415 prescribed length scale. The vertical mixing length used in this paper (100 m) was based on the  
416 sensitivity experiments of Bryan (2012). Prescribing a smaller mixing length produces smaller  
417  $\theta$  tendencies due to turbulence, but even with a mixing length on the low end of those tested  
418 by Bryan (2012), turbulence still played an important role in the tropopause-layer  $N^2$  evolution.  
419 Fig. A2 shows the 24-hour-averaged contributions of turbulent mixing to the  $N^2$  evolution from  
420 a simulation identical to that used in this paper, except with a vertical mixing length of 50 m. At  
421 all times, vertical turbulence still played an important role in the tropopause-layer  $N^2$  evolution,  
422 particularly during the latter stages of RI (48-72 hours).

## References

- Bryan, G. H., 2012: Effects of surface exchange coefficients and turbulence length scales on the intensity and structure of numerically simulated hurricanes. *Mon. Wea. Rev.*, **140**, 1125–1143.
- Bryan, G. H., cited 2018: The governing equations for CM1. [Available online at [http://www2.mmm.ucar.edu/people/bryan/cm1/cm1\\_equations.pdf](http://www2.mmm.ucar.edu/people/bryan/cm1/cm1_equations.pdf)].
- Bryan, G. H., and R. Rotunno, 2009: The maximum intensity of tropical cyclones in axisymmetric numerical model simulations. *Mon. Wea. Rev.*, **137**, 1770–1789.
- Bu, Y. P., R. G. Fovell, and K. L. Corbosiero, 2014: Influence of cloud-radiative forcing on tropical cyclone structure. *J. Atmos. Sci.*, **71**, 1644–1622.
- Doyle, J. D., and Coauthors, 2017: A view of tropical cyclones from above: The Tropical Cyclone Intensity (TCI) Experiment. *Bull. Amer. Meteor. Soc.*, **98**, 2113–2134.
- Duran, P., and J. Molinari, 2016: Upper-tropospheric low Richardson number in tropical cyclones: Sensitivity to cyclone intensity and the diurnal cycle. *J. Atmos. Sci.*, **73**, 545–554.
- Duran, P., and J. Molinari, 2018: Dramatic inner-core tropopause variability during the rapid intensification of Hurricane Patricia (2015). *Mon. Wea. Rev.*, **146**, 119–134.
- Emanuel, K., 2012: Self-stratification of tropical cyclone outflow. Part II: Implications for storm intensification. *J. Atmos. Sci.*, **69**, 988–996.
- Emanuel, K., and R. Rotunno, 2011: Self-stratification of tropical cyclone outflow. Part I: Implications for storm structure. *J. Atmos. Sci.*, **68**, 2236–2249.

442 Iacono, M. J., J. S. Delamere, E. J. Mlawer, M. W. Shephard, S. A. Clough, and W. D. Collins,  
 443 2008: Radiative forcing by long-lived greenhouse gases: Calculations with the AER radiative  
 444 transfer models. *J. Geophys. Res.*, **113** (D13103).

445 Kepert, J. D., J. Schwendike, and H. Ramsay, 2016: Why is the tropical cyclone boundary layer  
 446 not "well mixed"? *J. Atmos. Sci.*, **73**, 957–973.

447 Kieu, C., V. Tallapragada, D.-L. Zhang, and Z. Moon, 2016: On the development of double warm-  
 448 core structures in intense tropical cyclones. *J. Atmos. Sci.*, **73**, 4487–4506.

449 Kimberlain, T. B., E. S. Blake, and J. P. Cangialosi, 2016: Tropical cyclone report: Hurricane  
 450 Patricia. National Hurricane Center. [Available online at [www.nhc.noaa.gov](http://www.nhc.noaa.gov)].

451 Komaromi, W. A., and J. D. Doyle, 2017: Tropical cyclone outflow and warm core structure as  
 452 revealed by HS3 dropsonde data. *Mon. Wea. Rev.*, **145**, 1339–1359.

453 Markowski, P. M., and G. H. Bryan, 2016: LES of laminar flow in the PBL: A potential problem  
 454 for convective storm simulations. *Mon. Wea. Rev.*, **144**, 1841–1850.

455 Molinari, J., P. Duran, and D. Vollaro, 2014: Low Richardson number in the tropical cyclone  
 456 outflow layer. *J. Atmos. Sci.*, **71**, 3164–3179.

457 Ohno, T., and M. Satoh, 2015: On the warm core of a tropical cyclone formed near the tropopause.  
 458 *J. Atmos. Sci.*, **72**, 551–571.

459 Rogers, R. F., S. Aberson, M. M. Bell, D. J. Cecil, J. D. Doyle, J. Morgerman, L. K. Shay, and  
 460 C. Velden, 2017: Re-writing the tropical record books: The extraordinary intensification of  
 461 Hurricane Patricia (2015). *Bull. Amer. Meteor. Soc.*, **98**, 2091–2112.

462 Rotunno, R., and K. A. Emanuel, 1987: An air-sea interaction theory for tropical cyclones. Part II:  
463 Evolutionary study using a nonhydrostatic axisymmetric numerical model. *J. Atmos. Sci.*, **44**,  
464 542–561.

465 Stern, D. P., and F. Zhang, 2013: How does the eye warm? Part I: A potential temperature budget  
466 analysis of an idealized tropical cyclone. *J. Atmos. Sci.*, **70**, 73–89.

467 Thompson, G., R. M. Rasmussen, and K. Manning, 2004: Explicit forecasts of winter precipitation  
468 using an improved bulk microphysics scheme. Part I: Description and sensitivity analysis. *Mon.*  
469 *Wea. Rev.*, **132**, 519–542.

470 Trier, S. B., and R. D. Sharman, 2009: Convection-permitting simulations of the environment sup-  
471 porting widespread turbulence within the upper-level outflow of a mesoscale convective system.  
472 *Mon. Wea. Rev.*, **137**, 1972–1990.

## LIST OF FIGURES

- Fig. 1.** The maximum 10-m wind speed (top panel;  $\text{m s}^{-1}$ ) and minimum sea-level pressure (bottom panel; hPa) in the simulated storm (blue lines; plotted every minute) and from Hurricane Patricia's best track (red stars; plotted every six hours beginning at the time Patricia attained tropical storm intensity). The rapid weakening during the later stage of Patricia's lifetime was induced by landfall. . . . . 26
- Fig. 2.** Left panels: Twenty-four-hour changes in squared Brunt-Väisälä frequency ( $N^2$ ;  $10^{-4} \text{ s}^{-2}$ ) computed using Eq. 8 over (top row) 0-24 hours, (middle row) 24-48 hours, (bottom row) 48-72 hours. Middle Panels: The  $N^2$  change over the same time periods computed using Eqs. 4-7, Right Panels: The budget residual over the same time periods, computed by subtracting the budget change (middle column) from the model change (left column). Orange lines represent the cold-point tropopause height averaged over the same time periods. . . . . 27
- Fig. 3.** Time series of the contribution of each of the budget terms to the time tendency of the squared Brunt-Väisälä frequency ( $N^2$ ;  $10^{-4} \text{ s}^{-2}$ ). For each budget term, the absolute value of the  $N^2$  tendency is averaged temporally over 1-hour periods (using output every minute), and spatially in a region extending from 0 to 200 km radius and 14 to 21 km altitude. . . . . 28
- Fig. 4.** Twenty-four-hour averages of squared Brunt-Väisälä frequency ( $N^2$ ;  $10^{-4} \text{ s}^{-2}$ ) over (a) 0-24 hours, (b) 24-48 hours, (c) 48-72 hours. Orange lines represent the cold-point tropopause height averaged over the same time periods. . . . . 29
- Fig. 5.** (a) Total change in  $N^2$  over the 0-24-hour period ( $10^{-4} \text{ s}^{-2} (24 \text{ h})^{-1}$ ) and the contributions to that change from (b) the sum of horizontal and vertical advection, (c) vertical turbulence, (d) longwave and shortwave radiation, (e) the sum of horizontal advection, vertical advection, and vertical turbulence, and (f) the sum of horizontal advection, vertical advection, vertical turbulence, and longwave and shortwave radiation. Orange lines represent the cold-point tropopause height averaged over the 0-24-hour period. . . . . 31
- Fig. 6.** As in Fig. 5, but for the 24-48-hour period. . . . . 32
- Fig. 7.** As in Fig. 5, but for the 48-72-hour period. . . . . 33
- Fig. 8.** The contributions to the change in  $N^2$  over the 24-48-hour period ( $10^{-4} \text{ s}^{-2} (24 \text{ h})^{-1}$ ) by (a) horizontal advection and (b) vertical advection. (c) The radial velocity ( $\text{m s}^{-1}$ ; filled contours), potential temperature (K; thick black contours), cold-point tropopause height (orange line), and level of maximum outflow (dashed cyan line) averaged over the 24-48-hour period. (d) The vertical velocity ( $\text{cm s}^{-1}$ ; filled contours), potential temperature (K; thick black contours), and cold-point tropopause height (orange line) averaged over the 24-48-hour period. 34
- Fig. 9.** Ice mixing ratio ( $\text{g kg}^{-1}$ ) and cold-point tropopause height (orange lines) averaged over (a) 0-24 hours, (c) 24-48 hours, and (e) 48-72 hours. Radiative heating rate ( $\text{K h}^{-1}$ ) and cold-point tropopause height (orange lines) averaged over (b) 0-24 hours, (d) 24-48 hours, and (f) 48-72 hours. . . . . 36
- Fig. 10.** Idealized schematic diagram of turbulent mixing in a stably-stratified layer. At the initial time (left panel), potential temperature increases with height at a constant rate (thick black line). The imposition of turbulence within a portion of the layer (blue hatching) adjusts the potential temperature profile toward the mean initial value of that layer. After a period of



515	mixing (right panel) the potential temperature in the mixed layer does not vary with height,	
516	but just above and just below the mixed layer, it rapidly increases with height. . . . .	37
517	<b>Fig. 11.</b> Vertical eddy diffusivity ( $\text{m}^2 \text{s}^{-2}$ ; filled contours), cold-point tropopause height (cyan lines),	
518	and radial velocity ( $\text{m s}^{-1}$ ; thick black lines) averaged over (a) 0-24 hours, (b) 24-48 hours,	
519	and (c) 48-72 hours. . . . .	38
520	<b>Fig. 12.</b> (Top panel) Change in $N^2$ over the 24-48-hour period ( $10^{-4} \text{s}^{-2} (24 \text{ h})^{-1}$ ) directly output by	
521	the model for the 0-21-km layer. (Middle panel) Vertical eddy diffusivity ( $\text{m}^2 \text{s}^{-2}$ averaged	
522	over the same time period. (Bottom panel) Radiative heating rate ( $\text{K h}^{-1}$ ) averaged over the	
523	same time period. . . . .	40
524	<b>Fig. A1.</b> Twenty-four-hour averages of squared Brunt-Väisälä frequency ( $N^2$ ; $10^{-4} \text{s}^{-2}$ ) over (a) 0-24	
525	hours, (b) 24-48 hours, (c) 48-72 hours, and (d) 72-96 hours for the simulation described	
526	in Appendix Aa. Orange lines represent the cold-point tropopause height averaged over the	
527	same time periods. . . . .	41
528	<b>Fig. A2.</b> The contribution of vertical turbulence to the $N^2$ variability ( $10^{-4} \text{s}^{-2} (24 \text{ h})^{-1}$ ) averaged	
529	over (a) 0-24 hours, (b) 24-48 hours, (c) 48-72 hours, and (d) 72-96 hours for the simulation	
530	described in Appendix Ab. Orange lines represent the cold-point tropopause height averaged	
531	over the same time periods. . . . .	42

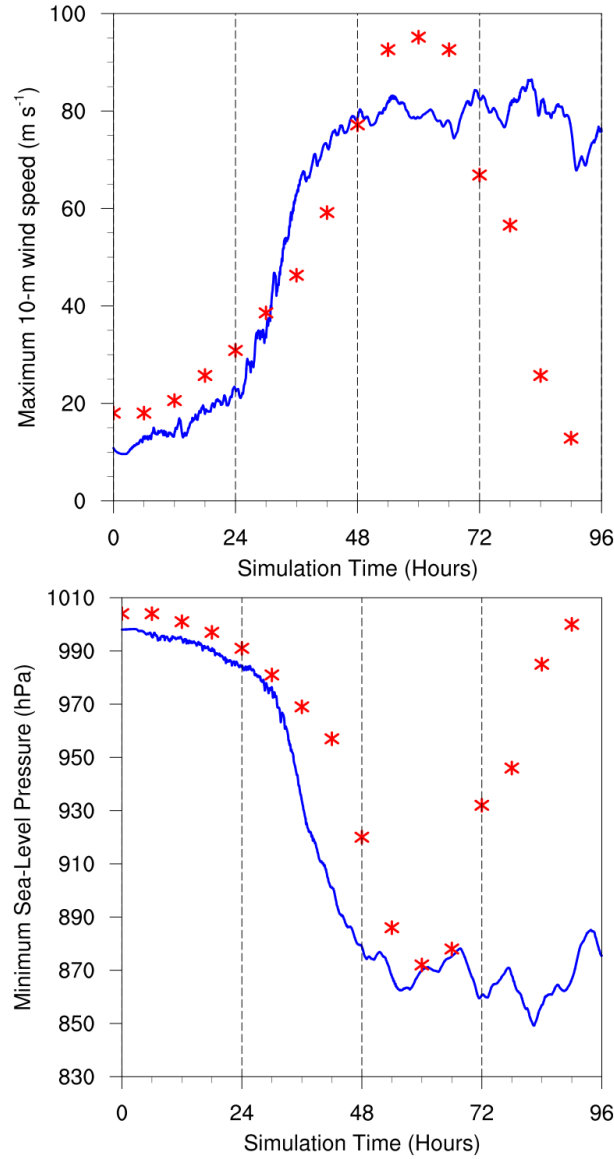


FIG. 1. The maximum 10-m wind speed (top panel;  $\text{m s}^{-1}$ ) and minimum sea-level pressure (bottom panel; hPa) in the simulated storm (blue lines; plotted every minute) and from Hurricane Patricia's best track (red stars; plotted every six hours beginning at the time Patricia attained tropical storm intensity). The rapid weakening during the later stage of Patricia's lifetime was induced by landfall.

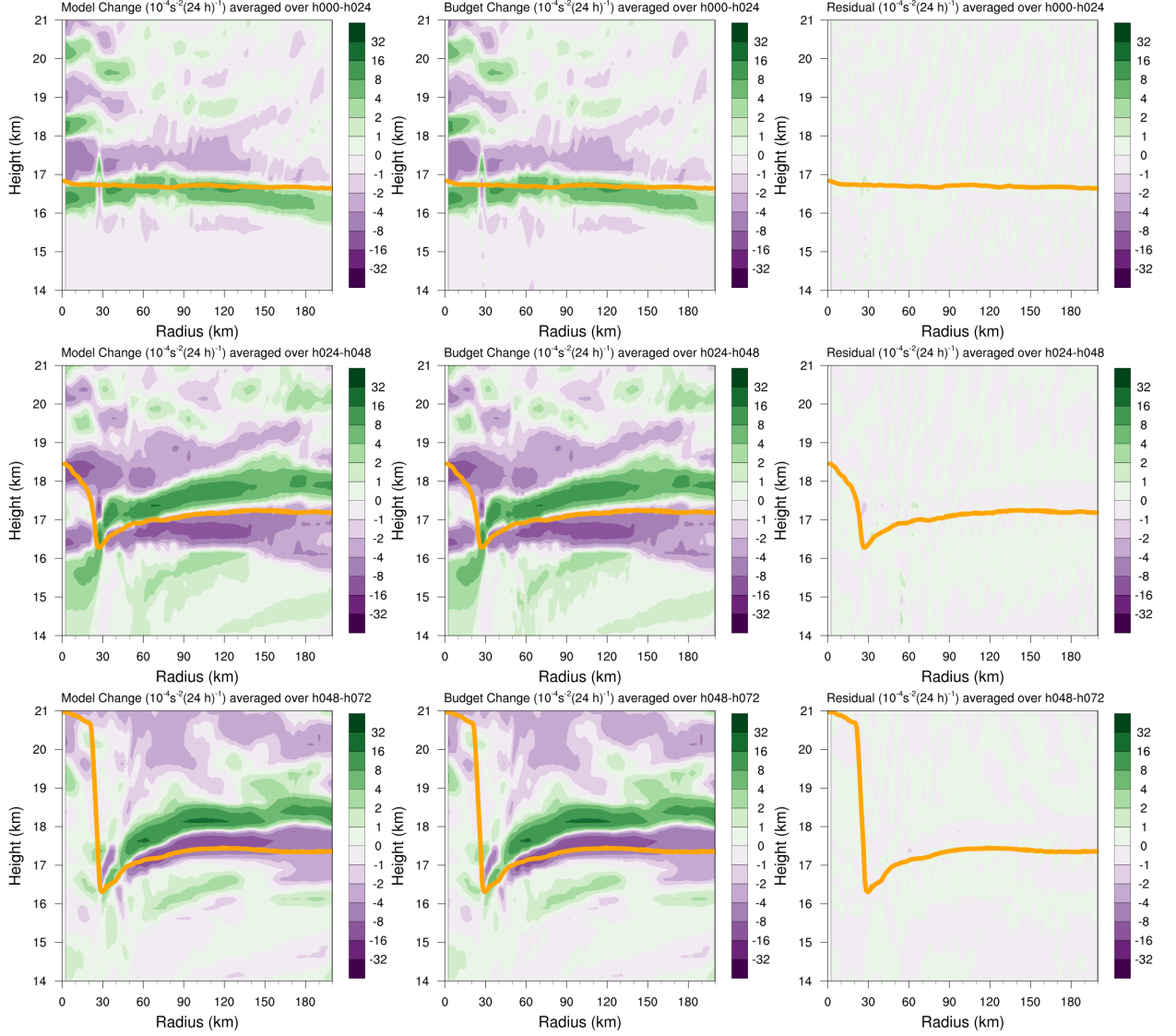


FIG. 2. Left panels: Twenty-four-hour changes in squared Brunt-Väisälä frequency ( $N^2$ ;  $10^{-4} \text{ s}^{-2}$ ) computed using Eq. 8 over (top row) 0-24 hours, (middle row) 24-48 hours, (bottom row) 48-72 hours. Middle Panels: The  $N^2$  change over the same time periods computed using Eqs. 4-7, Right Panels: The budget residual over the same time periods, computed by subtracting the budget change (middle column) from the model change (left column). Orange lines represent the cold-point tropopause height averaged over the same time periods.

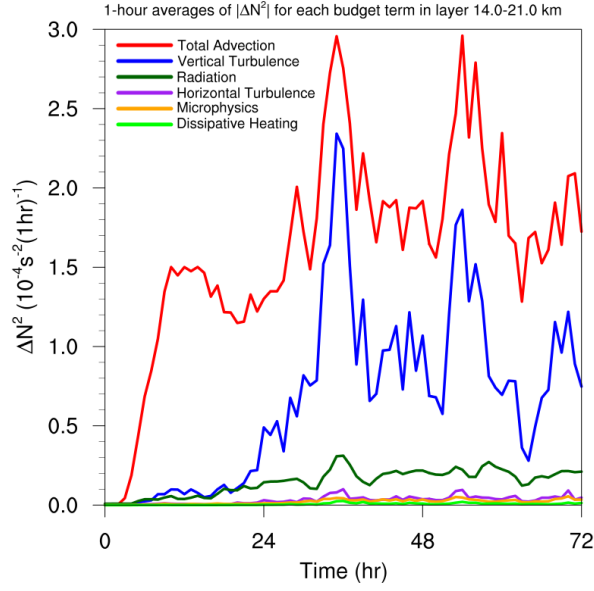


FIG. 3. Time series of the contribution of each of the budget terms to the time tendency of the squared Brunt-Väisälä frequency ( $N^2$ ;  $10^{-4} \text{ s}^{-2}$ ). For each budget term, the absolute value of the  $N^2$  tendency is averaged temporally over 1-hour periods (using output every minute), and spatially in a region extending from 0 to 200 km radius and 14 to 21 km altitude.

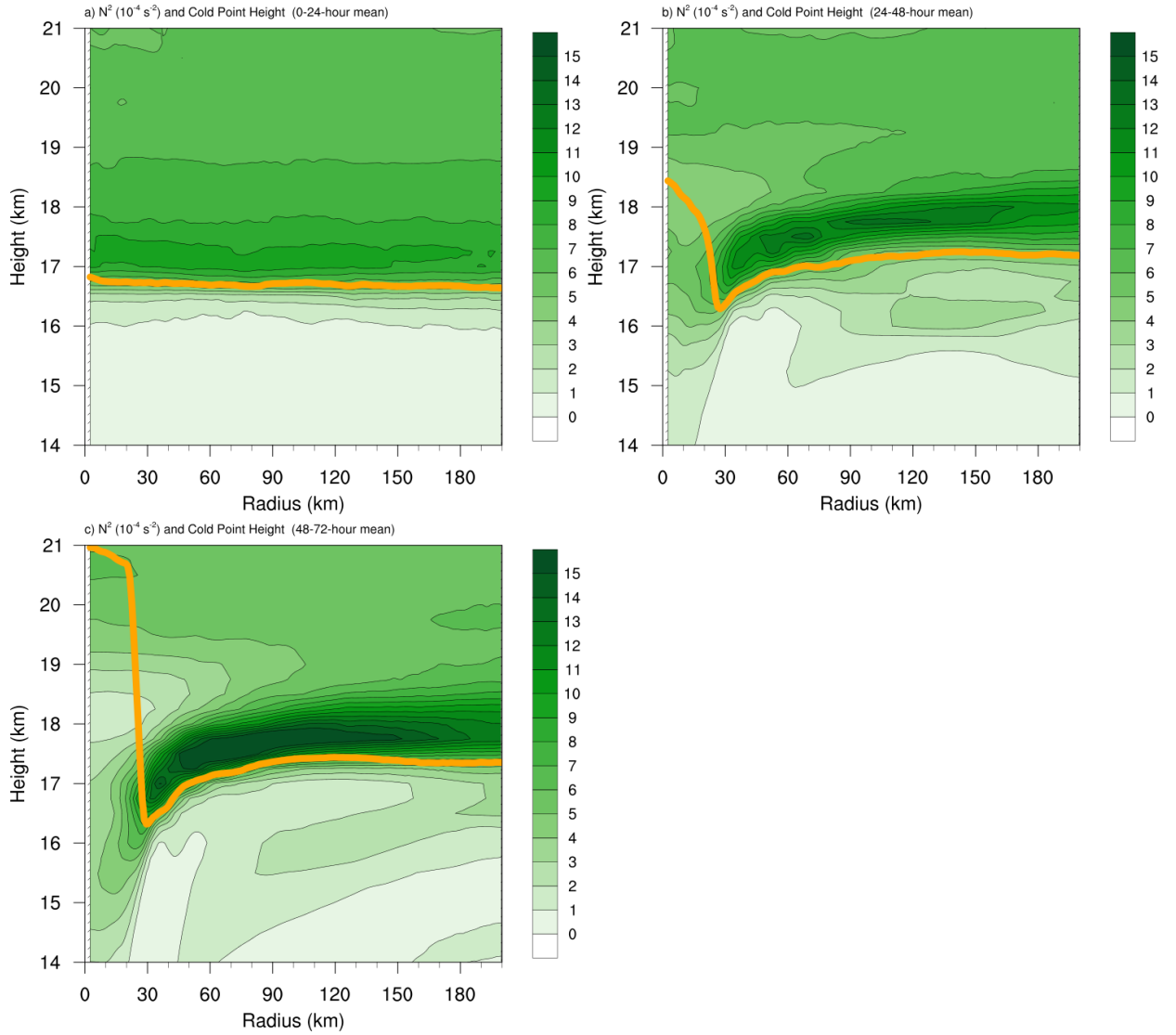
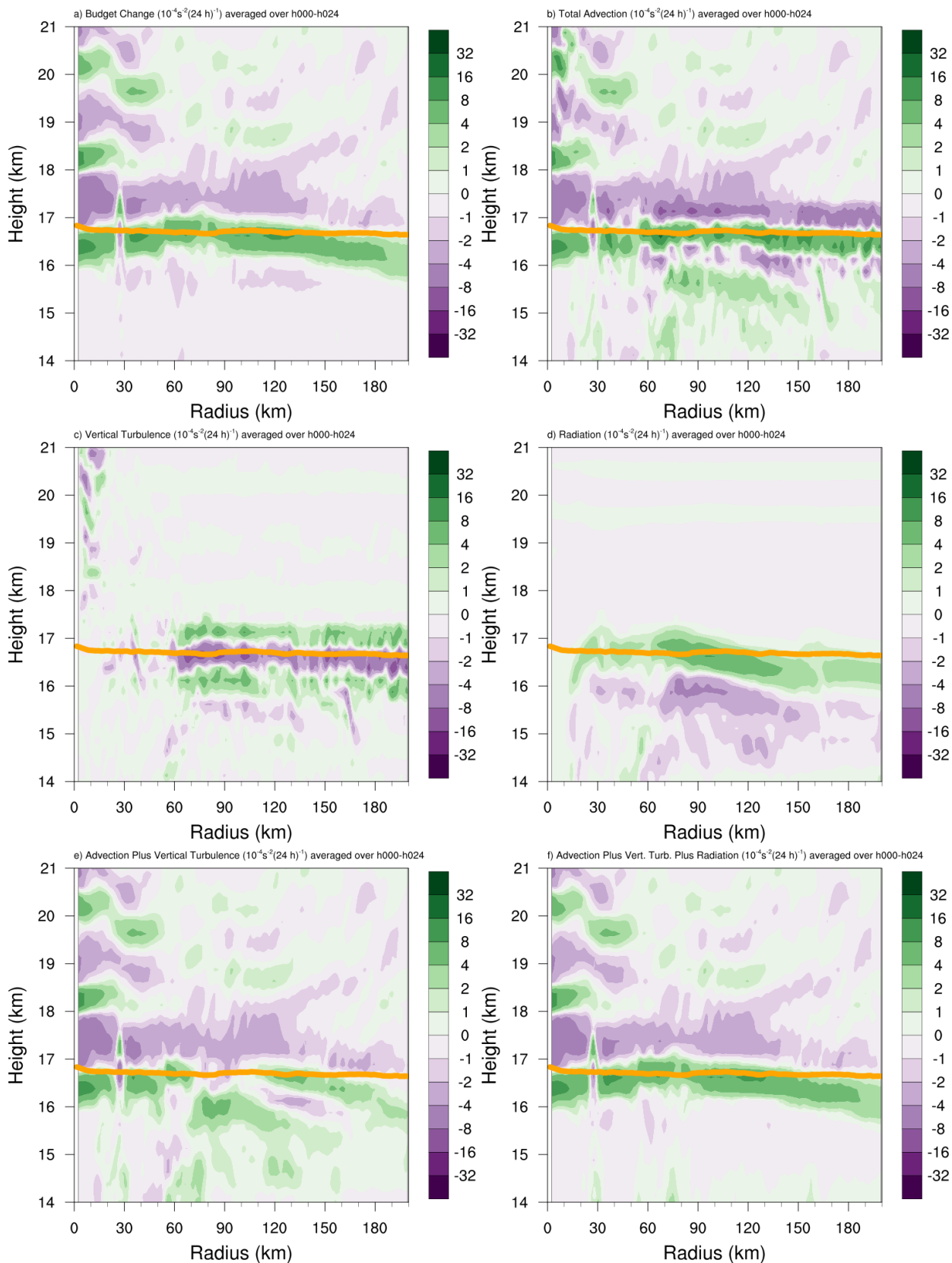


FIG. 4. Twenty-four-hour averages of squared Brunt-Väisälä frequency ( $N^2$ ;  $10^{-4} \text{ s}^{-2}$ ) over (a) 0-24 hours, (b) 24-48 hours, (c) 48-72 hours. Orange lines represent the cold-point tropopause height averaged over the same time periods.



548 FIG. 5. (a) Total change in  $N^2$  over the 0-24-hour period ( $10^{-4} \text{ s}^{-2} (24 \text{ h})^{-1}$ ) and the contributions to that change  
 549 from (b) the sum of horizontal and vertical advection, (c) vertical turbulence, (d) longwave and shortwave  
 550 radiation, (e) the sum of horizontal advection, vertical advection, and vertical turbulence, and (f) the sum of  
 551 horizontal advection, vertical advection, vertical turbulence, and longwave and shortwave radiation. Orange  
 552 lines represent the cold-point tropopause height averaged over the 0-24-hour period.

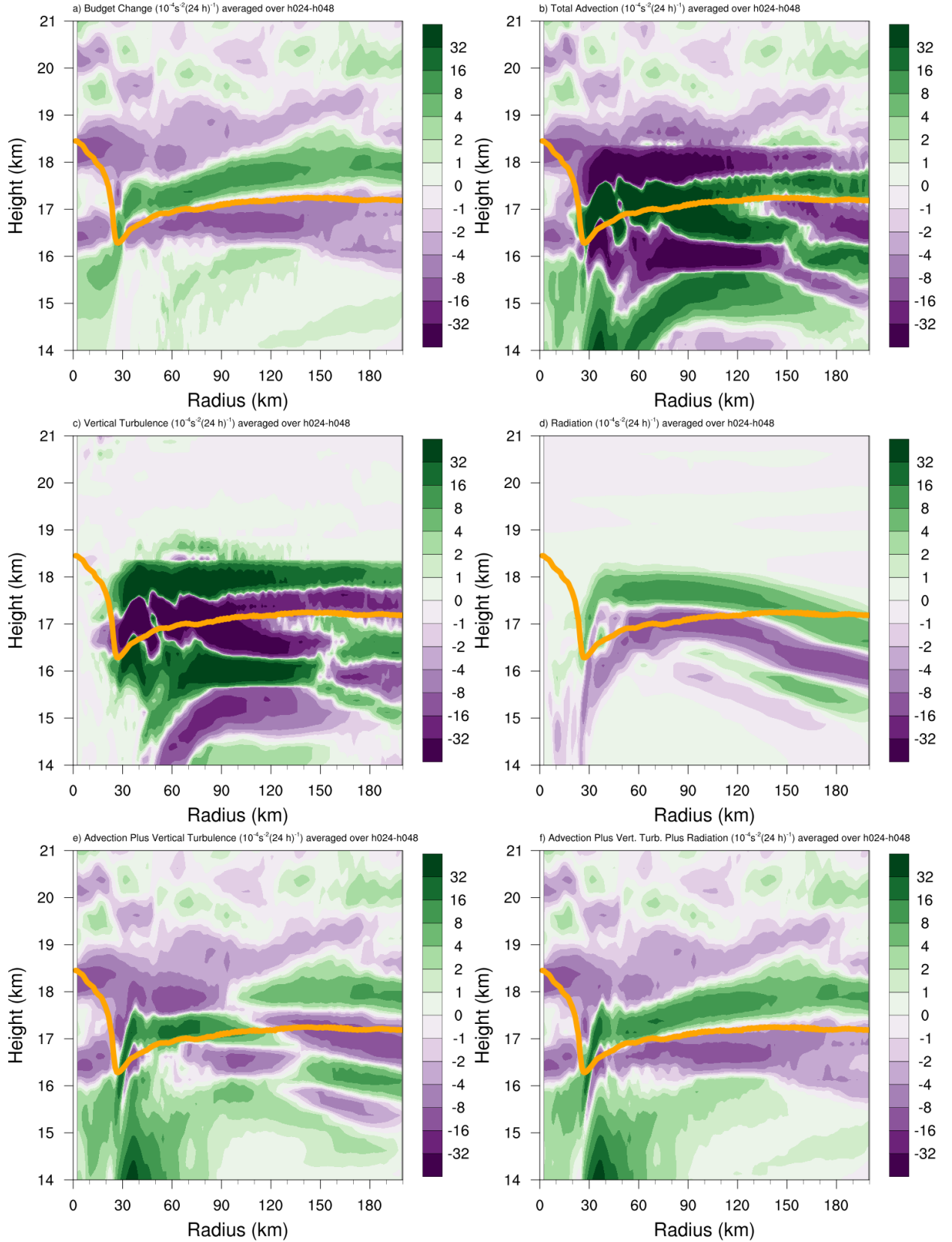


FIG. 6. As in Fig. 5, but for the 24-48-hour period.



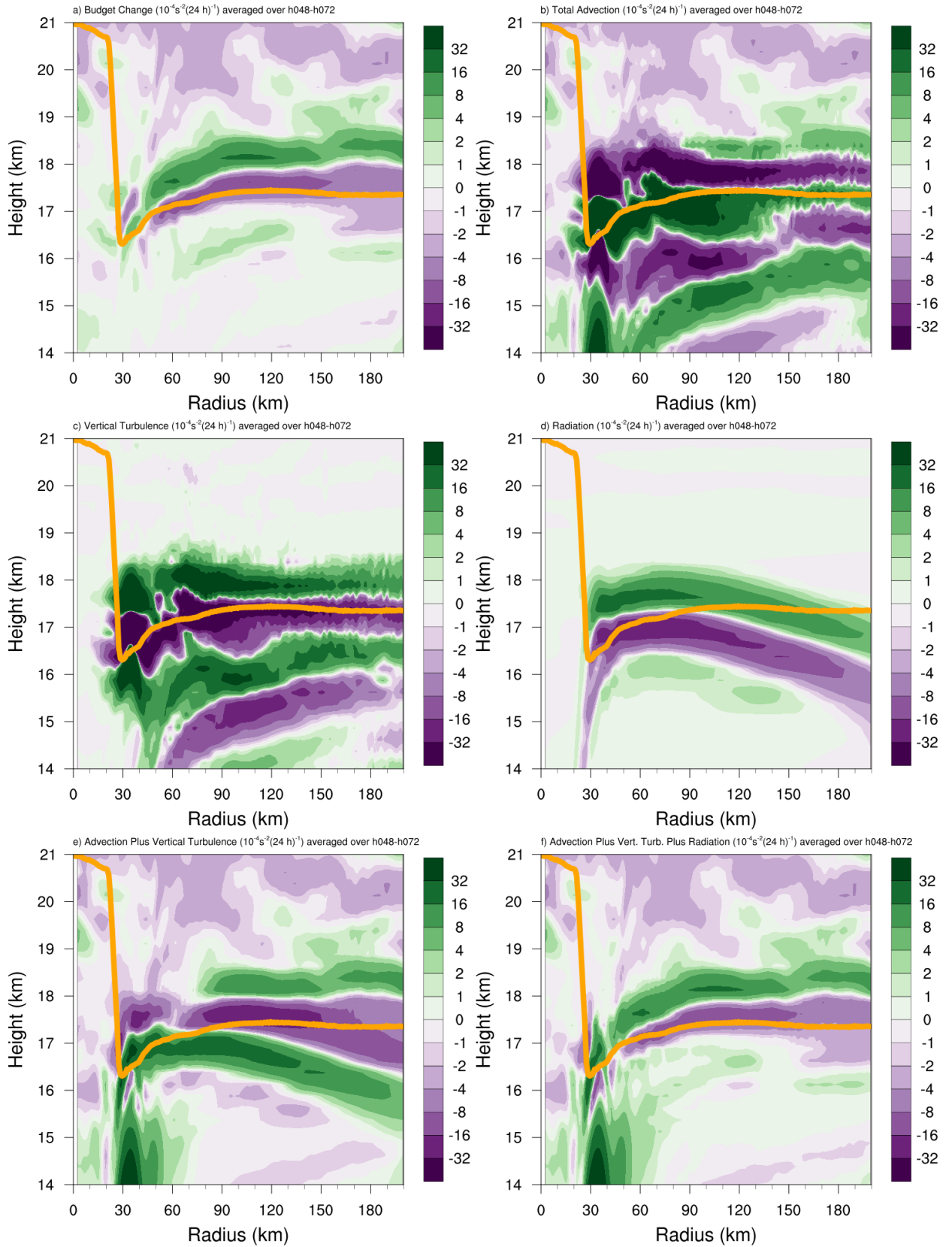


FIG. 7. As in Fig. 5, but for the 48-72-hour period.

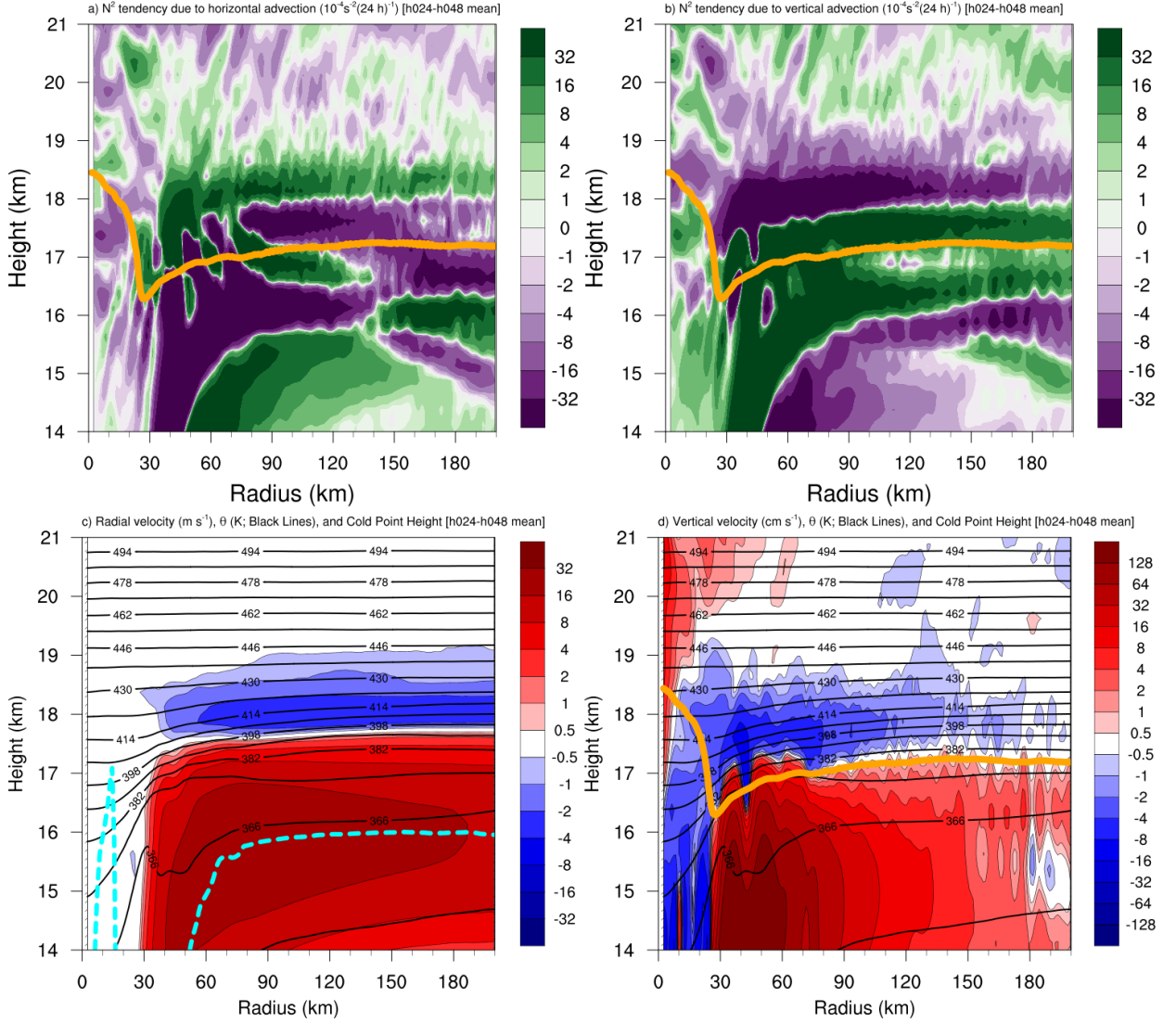
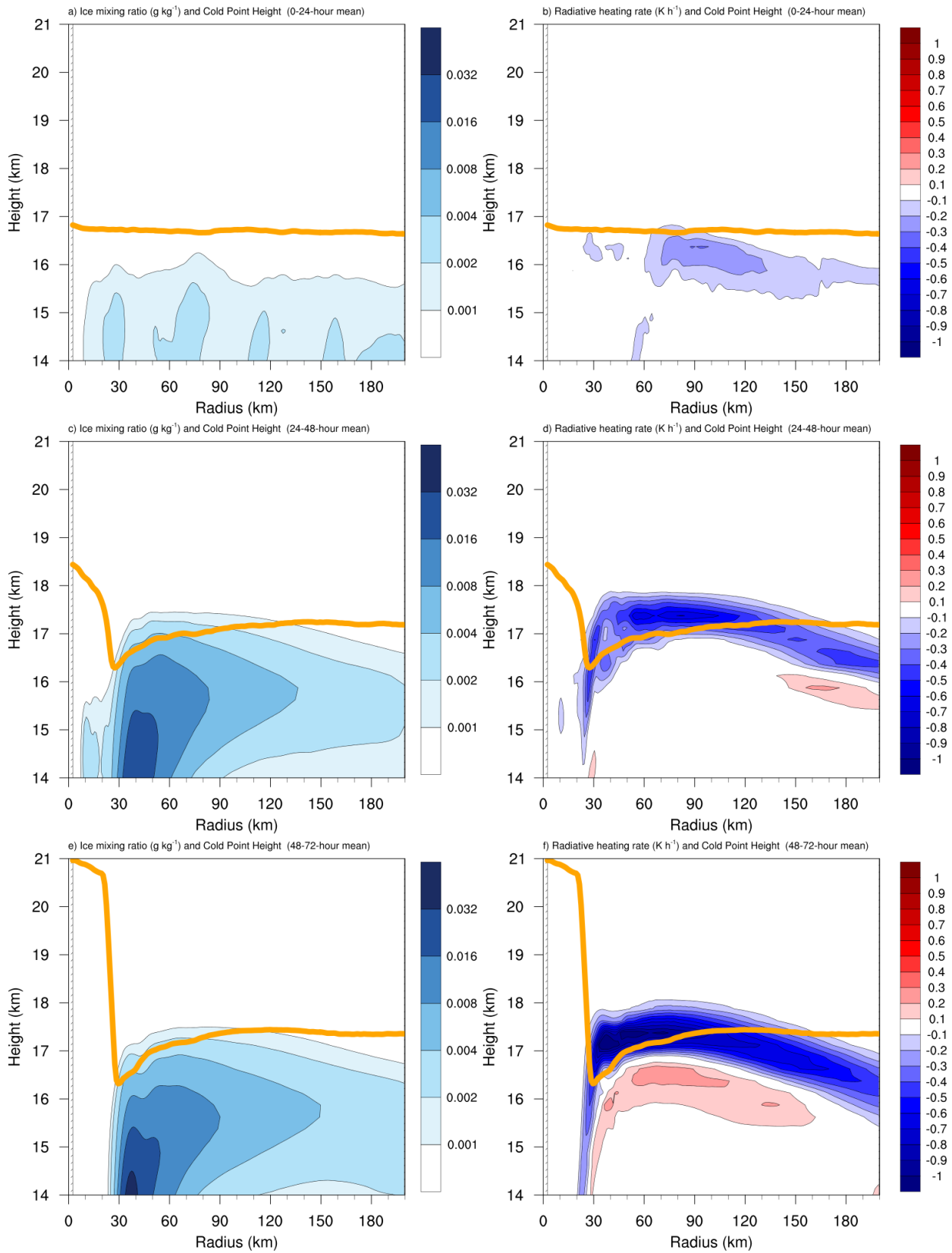


FIG. 8. The contributions to the change in  $N^2$  over the 24-48-hour period ( $10^{-4} \text{ s}^{-2} (24 \text{ h})^{-1}$ ) by (a) horizontal advection and (b) vertical advection. (c) The radial velocity ( $\text{m s}^{-1}$ ; filled contours), potential temperature (K; thick black contours), cold-point tropopause height (orange line), and level of maximum outflow (dashed cyan line) averaged over the 24-48-hour period. (d) The vertical velocity ( $\text{cm s}^{-1}$ ; filled contours), potential temperature (K; thick black contours), and cold-point tropopause height (orange line) averaged over the 24-48-hour period.



559 FIG. 9. Ice mixing ratio ( $\text{g kg}^{-1}$ ) and cold-point tropopause height (orange lines) averaged over (a) 0-24 hours,  
560 (c) 24-48 hours, and (e) 48-72 hours. Radiative heating rate ( $\text{K h}^{-1}$ ) and cold-point tropopause height (orange  
561 lines) averaged over (b) 0-24 hours, (d) 24-48 hours, and (f) 48-72 hours.

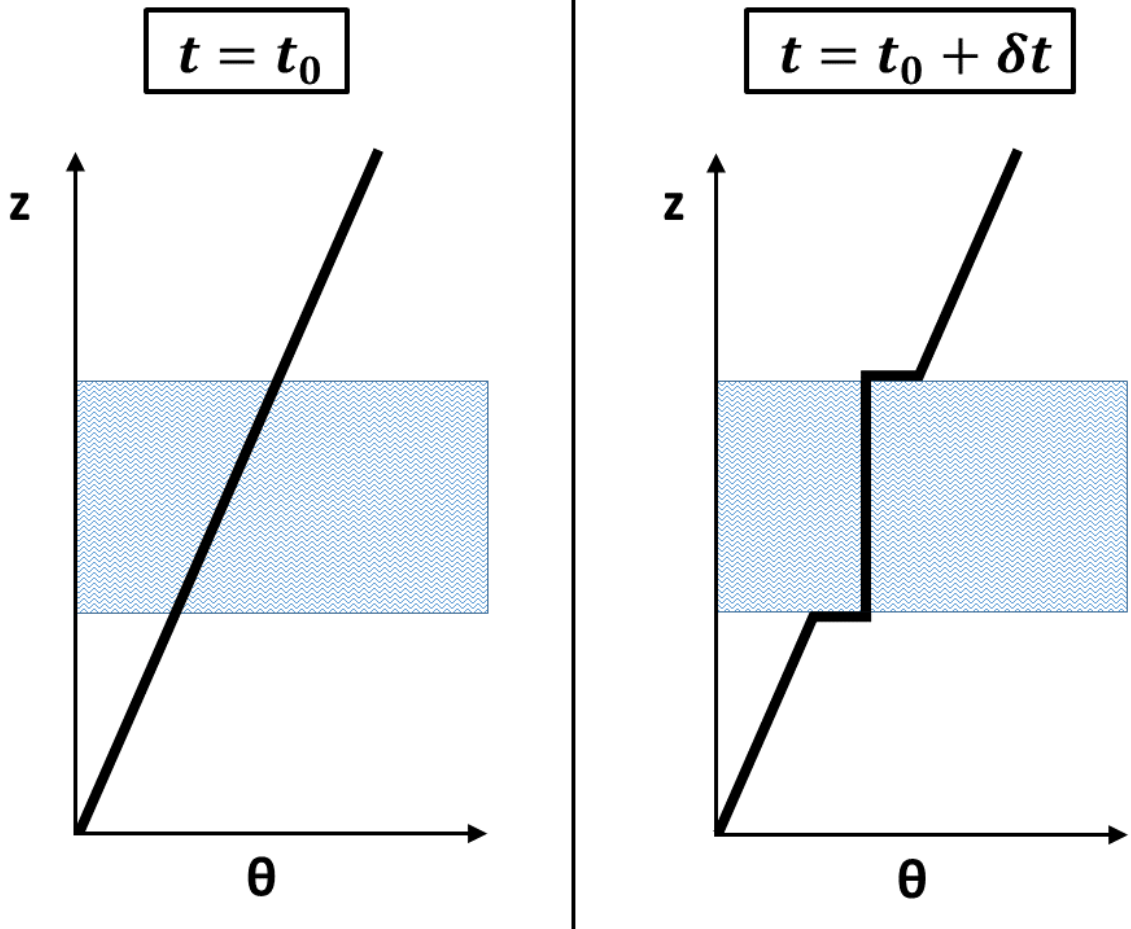


FIG. 10. Idealized schematic diagram of turbulent mixing in a stably-stratified layer. At the initial time (left panel), potential temperature increases with height at a constant rate (thick black line). The imposition of turbulence within a portion of the layer (blue hatching) adjusts the potential temperature profile toward the mean initial value of that layer. After a period of mixing (right panel) the potential temperature in the mixed layer does not vary with height, but just above and just below the mixed layer, it rapidly increases with height.

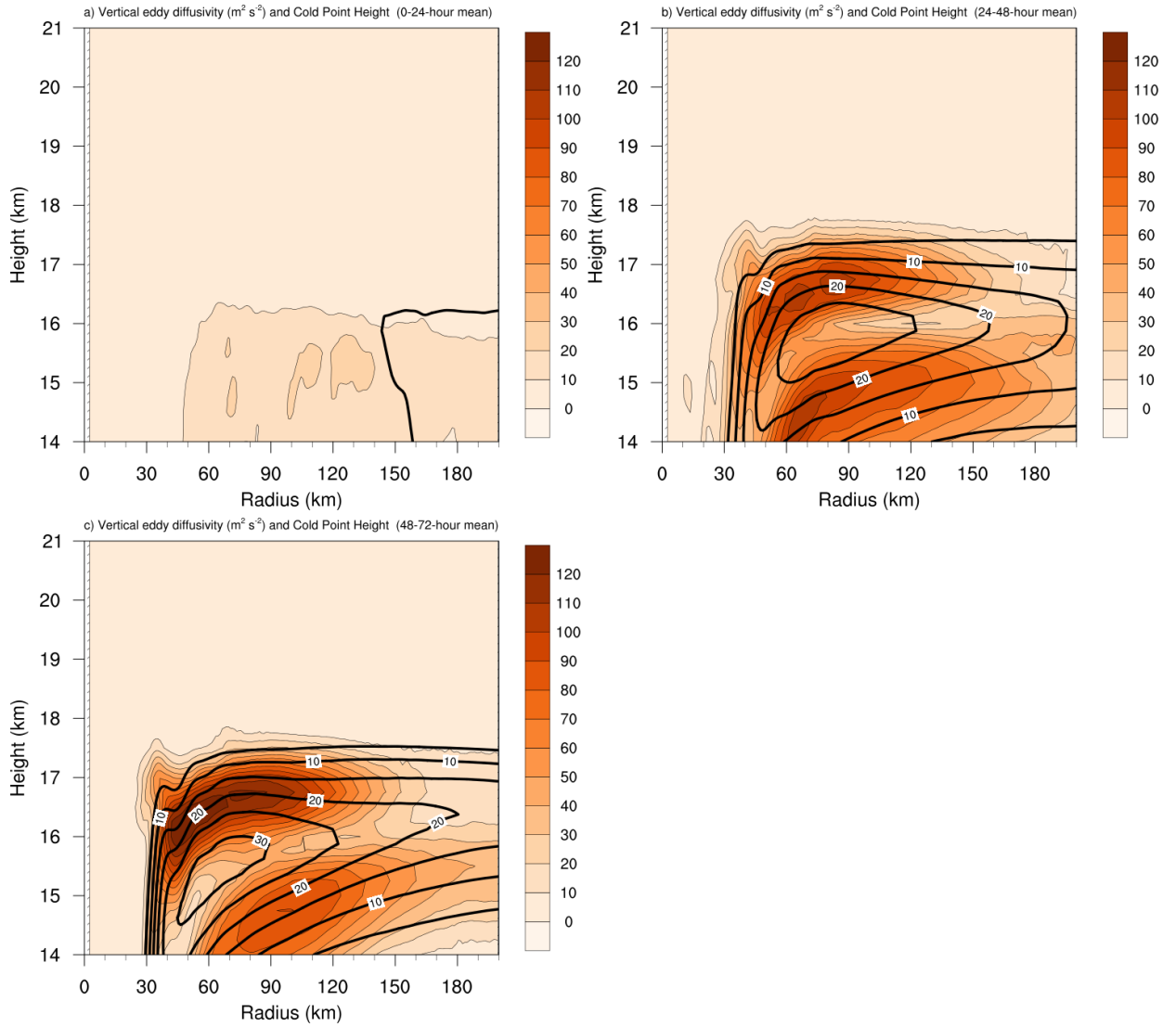
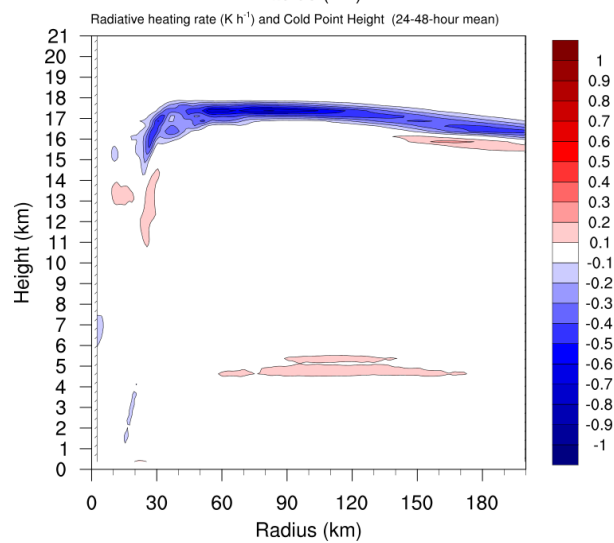
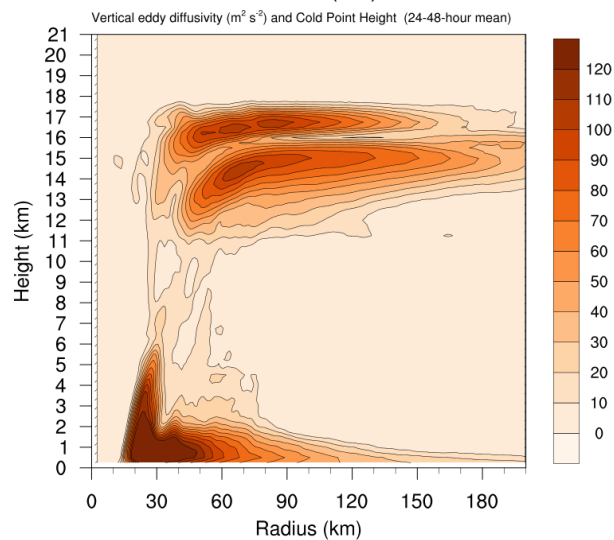
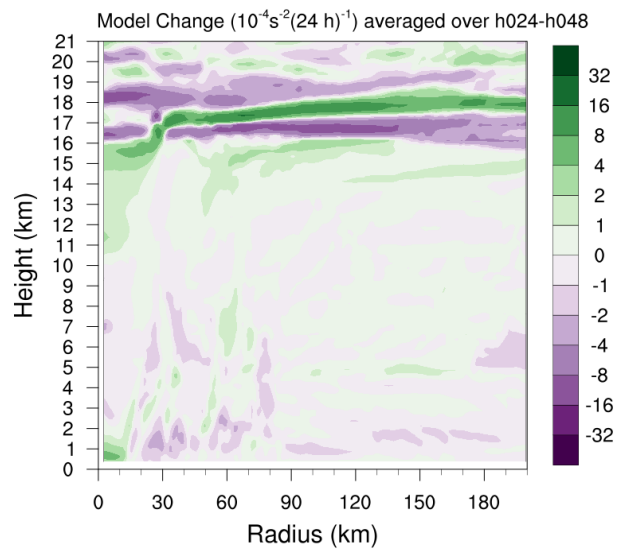


FIG. 11. Vertical eddy diffusivity ( $\text{m}^2 \text{s}^{-2}$ ; filled contours), cold-point tropopause height (cyan lines), and radial velocity ( $\text{m s}^{-1}$ ; thick black lines) averaged over (a) 0-24 hours, (b) 24-48 hours, and (c) 48-72 hours.



569 FIG. 12. (Top panel) Change in  $N^2$  over the 24-48-hour period ( $10^{-4} \text{ s}^{-2} (24 \text{ h})^{-1}$ ) directly output by the model  
570 for the 0-21-km layer. (Middle panel) Vertical eddy diffusivity ( $\text{m}^2 \text{ s}^{-2}$ ) averaged over the same time period.  
571 (Bottom panel) Radiative heating rate ( $\text{K h}^{-1}$ ) averaged over the same time period.



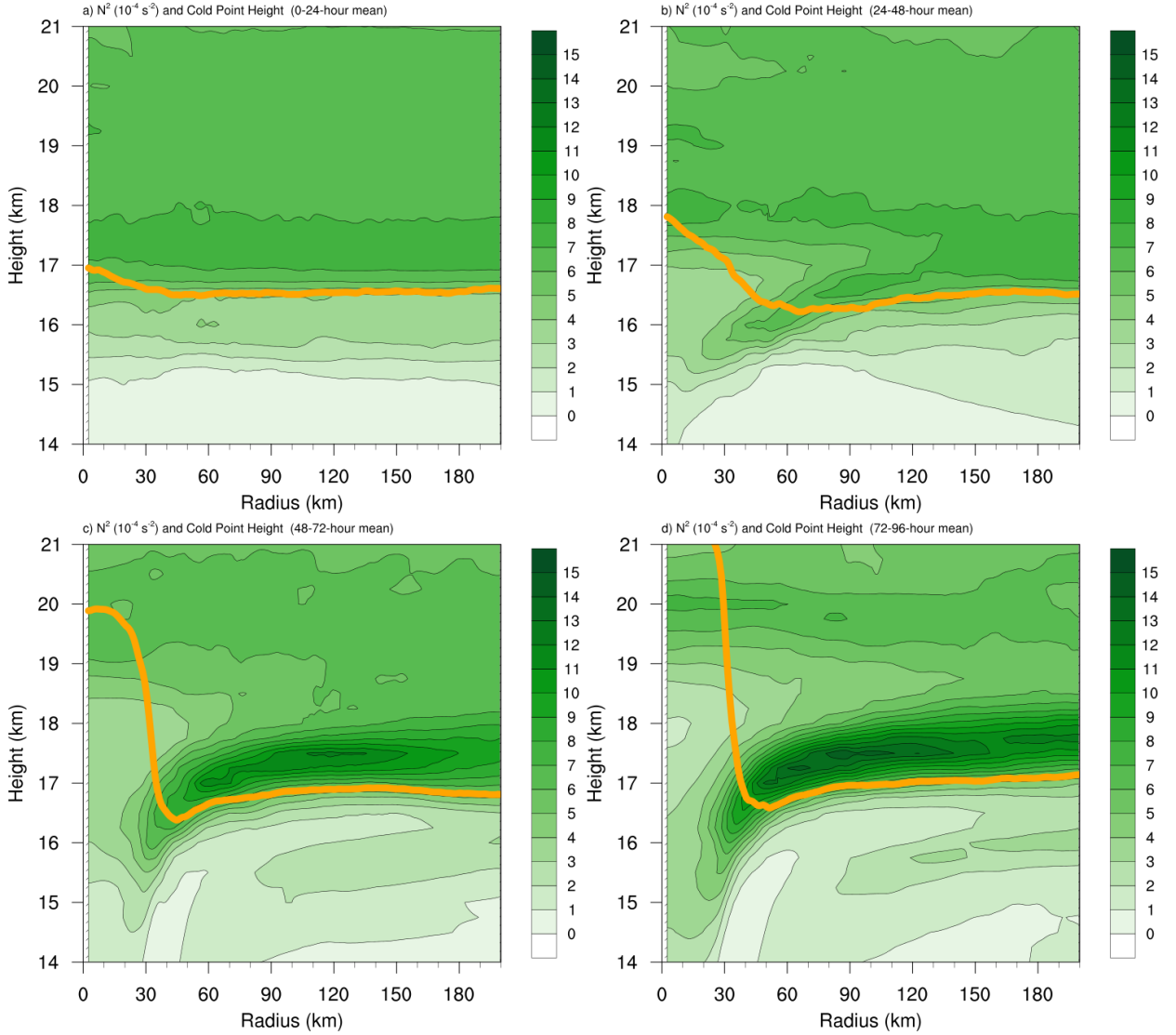


Fig. A1. Twenty-four-hour averages of squared Brunt-Väisälä frequency ( $N^2$ ;  $10^{-4} \text{ s}^{-2}$ ) over (a) 0-24 hours, (b) 24-48 hours, (c) 48-72 hours, and (d) 72-96 hours for the simulation described in Appendix Aa. Orange lines represent the cold-point tropopause height averaged over the same time periods.

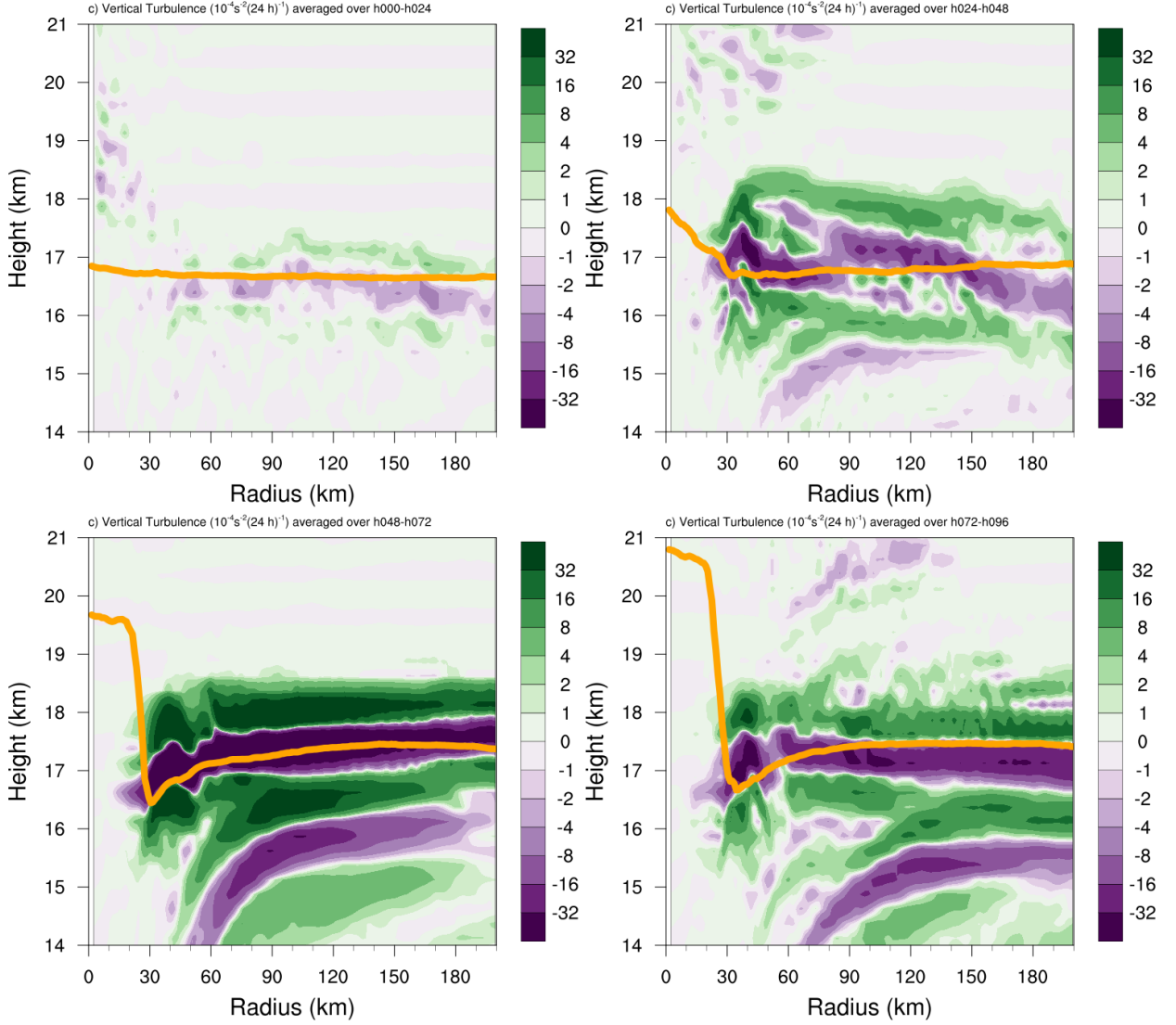


Fig. A2. The contribution of vertical turbulence to the  $N^2$  variability ( $10^{-4} \text{ s}^{-2} (24 \text{ h})^{-1}$ ) averaged over (a) 0-24 hours, (b) 24-48 hours, (c) 48-72 hours, and (d) 72-96 hours for the simulation described in Appendix Ab. Orange lines represent the cold-point tropopause height averaged over the same time periods.